WFIRST Technical Report
Doc #: WFIRST-STScI-TR1901
Rev: A
Date: February 13, 2019

WFIRST Wavelength Calibration: A Strategy with M67

R. E. Ryan Jr.[1], S. Casertano[1], S. Hernandez[1,2], A. Bellini[1], & N. Pirzkal[1]

rryan@stsci.edu

[1]Space Telescope Science Institute, Baltimore, MD 21218
[2]Radbound University, Nijmegen, The Netherlands

Abstract

We simulate a grism observation program to determine the fidelity of the wavelength calibration for the WFIRST/WFI instrument. To exploit the wide field-of-view, we consider observations of the open cluster M67 with a diameter of $\sim 25'$, but recent observations identify cluster members on degree scales. We find that near the cluster core, a WFIRST/WFI detector will contain ~ 100 kinematically-confirmed cluster stars. We measure the observed wavelength of the Paβ absorption line from these stars and find a typical percent error of $\sim 0.01\%$, which is sufficient for the needs of the cosmology experiments that need spectroscopic redshifts. We conclude with possible improvements to the M67 calibration plan, such as clusters of various ages/metallicities and more favorable celestial positions.

1 Introduction

The cosmology experiments with the Wide-Field Infrared Survey Telescope (WFIRST) to be performed with the High-Latitude Survey (HLS), expect accurate redshifts estimated from medium resolution grism spectroscopy ($R \sim 1000$). The WFIRST-AFTA final report requires a fractional uncertainty in $(1+z)$ of $\sigma_z/(1+z) \leq 0.001 - 0.005$ (Spergel *et al.* 2015). Naturally, this stringent requirement places equally demanding constraints on various calibration aspects.

Of particular importance in the calibration are the spectral trace and wavelength solution, which govern the position and wavelength dependence of the dispersed spectra, respectively. In traditional terms, these properties are given as polynomials whose coefficients vary as

functions of the undispersed position (x_0, y_0) on the detector:

$$y(x; x_0, y_0) = \sum_i \alpha_i(x_0, y_0)\, x^i \quad (1)$$

$$\lambda(s; x_0, y_0) = \sum_i \beta_i(x_0, y_0)\, s^i \quad (2)$$

where $s = s(x)$ is the path length along the trace:

$$s(x) = \int_0^x \sqrt{1 + \left(\frac{\mathrm{d}y}{\mathrm{d}x'}\right)^2}\, \mathrm{d}x'. \quad (3)$$

Please refer to Ryan, Casertano, & Pirzkal (2018) for a more complete description of this formulation. In this scheme, the path length effectively serves as a parameter to modulate the trace and wavelength solution, however Pirzkal & Ryan (2017) have proposed a generalization that eliminates the path length as the relevant parameter. For the purposes of this report, we consider only the canonical formulation, which distills the question of calibration of trace and wavelength solution to the accuracy with which the coefficients $\{\alpha_i(x_0, y_0)\}$ and $\{\beta_i(x_0, y_0)\}$ can be measured from reference sources.

This report is organized as follows: § 2 presents a brief history and wisdom gained from existing grism calibration programs, § 3 proposes a calibration program targeting an open star cluster, § 4 describes the simulations and analysis of stellar absorption-line spectroscopy, and § 5 discusses our results in the context of the wavelength solution and considers improvements to our proposed calibration plan. Unless specifically stated, we quote all magnitudes in the AB system (Oke & Gunn 1983).

2 Historical Perspective

At present, there are primarily two functioning space-based instruments capable of slitless spectroscopy whose operations are relevant: The Advanced Camera for Surveys (ACS) and the Wide-Field Camera 3 (WFC3) — the latter of which has two distinct modes: UVIS and IR. The WFC3/IR observations cover roughly the same wavelengths ($0.8 - 1.7$ μm) as the WFIRST Wide-Field Imager (WFI), and so they provide the most insights to needed calibration procedures. Generally, there are three properties of interest: the wavelength solution (the lowest order term of which is the "wavelength zeropoint"), the spectral trace, and the sensitivity. Obviously, the wavelength requires a source with known observer-frame spectral features, and for WFC3/IR it is usually the marginally resolved planetary nebula VY2-2, which has emission from O I, [S III], and H I (Pa7, Br12, and Br13). Since this object is barely resolved and often saturates the core, it is not a viable calibrator for the trace or sensitivity. Therefore a white dwarf (usually GD 71) is used for the trace and sensitivity, but Pirzkal, Ryan, & Brammer (2016) presented a significant improvement on the spectral trace using the complete collection of all bright point sources observed by WFC3/IR over ~ 8 years. This ability to "multiplex" the calibration of the trace is important, as it saves critical observing time — particularly since these functions must be calibrated at many more

positions on the detector. Based on the Pirzkal, Ryan, & Brammer (2016) findings, we omit calibration of the spectral trace as this can be bootstrapped from the HLS observations if concurrent direct images are taken. Instead, we focus on the calibration of the wavelength zeropoint, as the typical field is unlikely to contain many sources with spectral features known *a priori*.

This approach of a single source placed at various positions is simply impractical for WFIRST/WFI, which will have 18 4k×4k detectors. In contrast, WFC3/IR has a single 1k×1k detector; hence to have the same spatial sampling of the calibration products as produced by the WFC3/IR Team, the WFIRST/WFI will require 288× more observing time. Additionally, the WFIRST/WFI will disperse at ~ 11 Å pix^{-1}, which is $\sim 2.5 - 5\times$ higher resolution than WFC3/IR. Although this comparison to the WFC3/IR calibration illuminates an order of magnitude estimate, it obviously skirts the question of whether or not the WFC3/IR calibrations are actually sufficient to meet the WFIRST/WFI demands, but it does set the order of magnitude for the calibration plan. Since the nominal calibration program would require ~ 0.5 year of observing, it is important to consider alternatives, particularly the ones that leverage the multiplexing afforded by slitless spectroscopy. But first it is worth describing the desirable properties of an ideal calibrating source:

bright: limits the exposure time required to achieve a desired signal-to-noise ratio;

narrow spectral features: improves estimates of the observed-frame wavelength;

unresolved: improves the line-spread function and eliminates any ambiguity in the region that emits the relevant spectral feature(s); and

common: provides multiplexing on a given detector and/or the entire array; and

multiple spectral features: needed to span the full wavelength coverage that is expected for the WFIRST spectroscopic element ($\sim 1 - 2$ μm with $\delta\lambda \sim 11$ Å pix^{-1}).

Based on these considerations, we propose that open star clusters might satisfy these many constraints, however this would require assessing the coefficients $\{\beta_i(x_0, y_0)\}$ based on stellar absorption lines. This represents a significant departure in calibration philosophy, which historically is based on the emission lines of planetary nebulæ. Therefore the primary motivation of this report is to examine the feasibility of using stellar absorption lines to calibrate the wavelength solution.

3 A Test Case: M67

M67 (NGC 2682) is a Galactic open cluster with an estimated diameter of $\sim 25'$ (Krone-Martins *et al.* 2010) and age of ~ 4 Gyr (Sarajedini 1999). Therefore the main-sequence turnoff corresponds to roughly stars of type G0V, hence there are a number of stars with strong Paschen and metallic absorption lines. Also, the relatively diffuse nature of the cluster means we can expect ~ 100 stars per WFI detector, which satisfies the multiplexing constraint, although it may require several pointings to fully sample all 18 detectors.

To identify cluster members distinct from field stars or background galaxies, we use the catalog presented by Yadav *et al.* (2008) to select point sources with a common proper

Table 1: Observed Properties of M67

Property	Value	Reference
age	3.9 Gyr	Bellini *et al.* (2010)
metallicity	[Fe/H] $\sim$ 0.06	Bellini *et al.* (2010)
line-of-sight velocity dispersion	$\sigma_R = 0.59^{+0.07}_{-0.06}$ km s^{-1}	Geller *et al.* (2015)
angular diameter	$\theta \sim 25'$	Krone-Martins *et al.* (2010)
distance	$(m-M)_0 \sim 9.7$ mag	Sarajedini *et al.* (2009)
brightness of main-sequence turnoff	$V \sim 13.5$ mag	Yadav *et al.* (2008)
reddening	$A_V \sim 0.094$ mag	Schlafly & Finkbeiner (2011)
coordinates	Equatorial 132.°8339 +11.°8120	
	Ecliptic 131.°9651 −5.°6076	
	Galactic 215.°6875 +31.°9092	

motion[1]. In Figure 1, we show the relative proper motion for all of the Yadav *et al.* sources with $\mu \leq 2$ milliarcsec yr^{-1} (red circle) as selected cluster members. From these sources, we construct the optical color-magnitude diagram (CMD) in Figure 2. From this we identify 318 confirmed cluster members with $V \leq 21$ Johnson mag. As a final note, we do not anticipate any significant changes in our findings by using the *Gaia*-DR2 data since the improvement in the astrometric positions are much smaller than the pixel size of the WFI detector. Moreover, the *Gaia*-DR2 photometry does not identify significantly more cluster members (see Figure 3 for a comparison between *Gaia*-DR2 and Yadav *et al.* (2008)).

4 WFI Grism Observations

4.1 Grism Simulations

We generate an idealized direct image of the M67 field using positions, effective temperatures, and surface gravities for the known cluster members from the Yadav *et al.* (2008) catalog. We assume the image is taken through the H-band, as this band is fully sampled by the grism element[2] (see Figure 4). In practice, this direct image can be obtained by a multi-epoch campaign, however some data taken contemporaneously to the grism exposures to improve the astrometry is generally wise (as is the stated policy for HST/WFC3 grism observations). The final observing strategy for the WFIRST HLS is still under active discussion, and so we recognize that this plan may change. Ultimately, the timeline for the direct/grism observations is not relevant to the present study, but only concerns the accuracy with which the wavelength solution can be applied. We adopt a Gaussian PSF with a FWHM $= 0''.17$ (the diffraction limit for a 2.4 m aperture at 1.6 μm) and assume this direct image is oversampled with a pixel scale of $0''.06$ pix^{-1}.

[1] At the beginning of this investigation, the *Gaia*-DR2 catalog was not available, but in Figure 3 we show the comparison with Yadav *et al.* (2008)

[2] This assumption is not critical, but serves to improve the initial conditions for the spectral extraction.

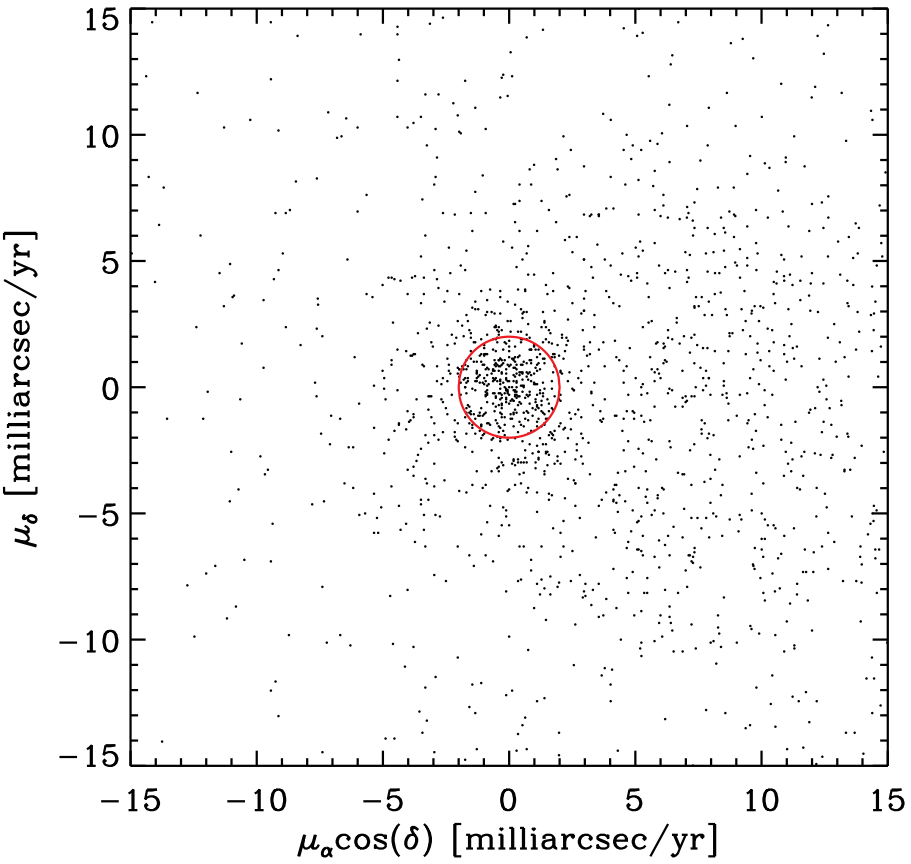

Figure 1: Relative proper motion for M67. These data are taken from Yadav *et al.* (2008). We select the group of stars with common proper motion, as indicated by the red circle. This selection results in 318 stars.

For synthetic stellar spectra, we generate atmospheric models with `ATLAS9` (Kurucz 1970) for a 4 Gyr simple stellar population with solar metallicity (*e.g.* Bellini *et al.* 2010) for stars with $T_{\rm eff} > 3500$ K. With these models, we compute individual stellar spectra with `SYNTHE` (Kurucz & Furenlid 1979; Kurucz & Avrett 1981) for $1 - 2$ μm sampled every 0.01 Å. We use `LINEAR` (Ryan, Casertano, & Pirzkal 2018) to simulate a noiseless grism image, assuming a unity flat field and pixel-area map with the grism calibration given in Appendix A. To account for noise, we describe the uncertainty in each pixel (x, y) in units of e^- as:

$$\sigma_{x,y} = \sqrt{(\mathcal{D} + \mathcal{B} + \mathcal{S}_{x,y})\, t + \mathcal{R}_{\rm eff}^2}, \tag{4}$$

where $\mathcal{D}$ is the dark current, $\mathcal{S}_{x,y}$ is the noiseless image simulated by `LINEAR`, $\mathcal{B}$ is the effective sky background (described more in more detail below), t is the exposure time, and $\mathcal{R}_{\rm eff}$ is the effective readnoise. We scale the effective readnoise for 15 reads following the WFC3/IR expectation (see Figure 5.25 of the WFC3 Handbook[3]). We do not consider or model any effects associated with saturation of the brightest stars, as we expect these to be a minority of the sample (see Figure 2). From experience with WFC3, we expect saturated stars can be recovered in partial ramp samplings, or in the case of extreme saturation, masked/omitted from additional analyses. We present the assumed detector properties in Table 2.

In principle, the effective sky background in a grism exposure is quite complex since each spectral order may contribute to every pixel. However, there are generally baffles that

[3] http://www.stsci.edu/hst/wfc3/documents/handbooks/currentIHB/

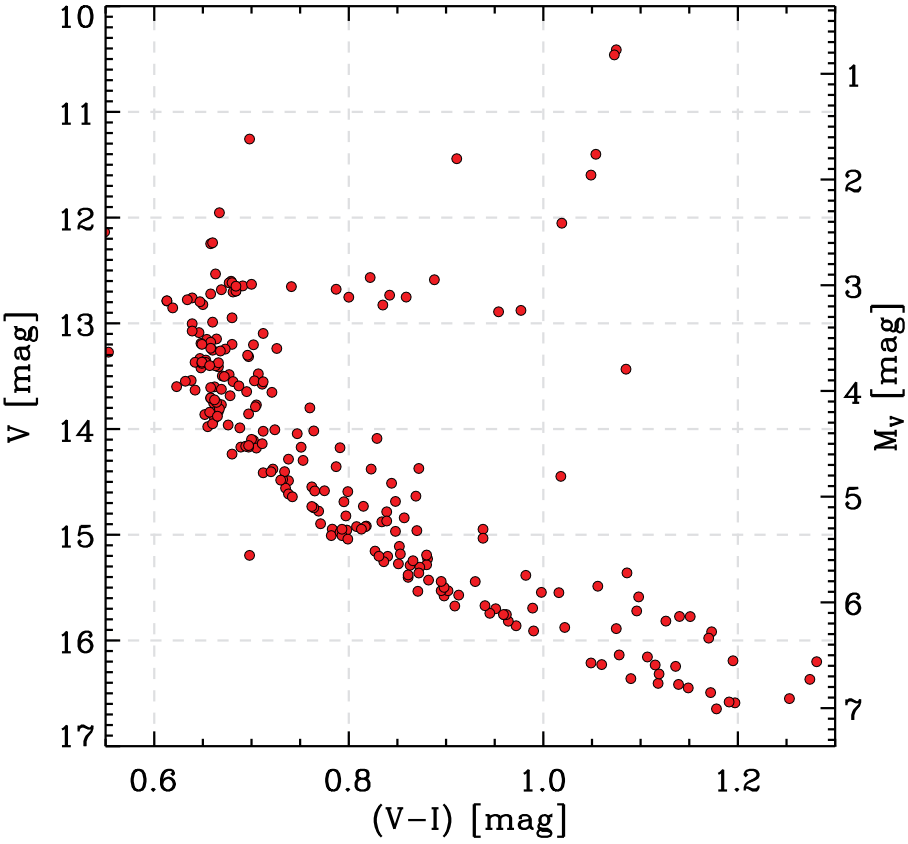

Figure 2: Optical color-magnitude diagram for M67. These data are taken from Yadav *et al.* (2008), but after our proper motion selection described in Figure 1. We further cull this list by requiring $V \leq 17$ mag (in Johnson units). Therefore, our final catalog of M67 contains 267 relatively bright stars as cluster members.

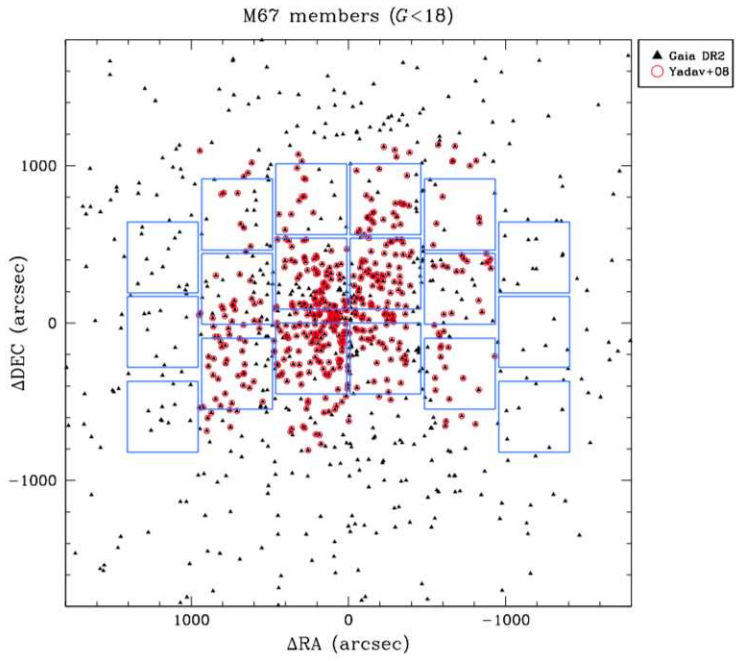

Figure 3: Comparison between Yadav *et al.* (2008; red circles) with *Gaia*-DR2 (Gaia collaboration 2018; black triangles) for $G < 18$ mag. Here the local (on the scale of a WFI detector) and global (the WFI array) source density is easily seen, which suggests a 2×1 pointing strategy will provide calibration for all 18 detectors. In the core of the cluster, the Yadav *et al.* (2008) catalog is reasonably complete (compared to *Gaia*) but is limited to the inner $\sim 33' \times 32'$ (roughly $\sim 2000'' \times 2000''$). These *Gaia* results do not significantly affect our work, but illustrate the multiplexing that will be possible with M67.

restrict the distance from the detector that a source (or patch of sky in this case) may be, and still contribute to the sky. Furthermore, faint, unresolved cluster members may contribute some excess light, likely redder than the detected members. These effects lead to a distinct spatial structure in the grism sky backgrounds, which is *independent* of the flat field. Therefore, a full treatment of the sky background requires a detailed knowledge of the optical path, properties of the spectral orders, and the spectral characteristics of the effective sky spectrum. Since only the latter is knowable at this time, we defer a thorough simulation of the effective sky background to a later time, and instead opt to treat the sky as a constant pedestal applied to every pixel.

We expect that the effective sky background will largely come from two sources: zodiacal and thermal. The zodiacal background depends on the celestial position of the source and the time of year of the observation, whereas the thermal is regulated by the instrument and expected to be (roughly) constant. Rhoads *et al.* (in prep) find that zodiacal contribution to the sky background dominates the thermal for an operating temperature of $T = 260$ K. Therefore we only include the zodiacal term, which can be computed as an integral over the zodiacal spectrum ($f_{\mathcal{Z},\lambda}$), weighted by the sensitivity curve (S_λ):

$$\mathcal{Z} = \int S_\lambda \, f_{\mathcal{Z},\lambda} \, \mathrm{d}\lambda. \tag{5}$$

We adopt the zodiacal spectrum given by Giavalisco, Sahu, & Bohlin (2002) for $0.5 \leq \lambda \leq 2.5$ μm:

$$\left(\frac{f_{\mathcal{Z},\lambda}}{f_{0.5}}\right) \approx 1.0 + 0.48 \, \ln\left(\frac{\lambda}{0.5 \ \mu\mathrm{m}}\right) \tag{6}$$

where $f_{0.5}$ is the flux at $\lambda = 0.5$ μm, which they give as 1.8×10^{-18} erg s^{-1} cm^{-2} Å^{-1} arcsec^{-2}. As an additional note, this value is approximately the typical sky brightness expected from the JWST Exposure Time Calculator. Using the sensitivity curve shown in Figure 4, we estimate a sky background of $\mathcal{B} = 1.1$ e$^-$ s^{-1}. We caution, this should be regarded as a lower limit for several reasons (the multiple orders are not included, the thermal contribution was ignored, and M67 is at fairly low ecliptic latitude), however this will only affect the signal-to-noise on the spectra and, as we will show below, the absorption line wavelengths are extremely well constrained. The expected count from the sky background in a 350 s exposure is quite high ($\gtrsim 400$ e$^-$), therefore we approximate the Poisson distribution as Gaussian.

4.2 Grism Extractions

The goal of this report is to examine the viability of absorption-line spectroscopy of stellar cluster members as a means to calibrate the wavelength solution. From previous work with WFC3/IR, it is fairly straight-forward to determine the spatial dependence of the calibration (see Equation 2), provided the observed wavelengths of the spectral lines are reliably measured. Therefore, we concentrate on measuring the known spectral lines from the stellar atmospheres of the known cluster members. For simplicity, we only consider the *wavelength zeropoint*, which is given as $\beta_0(x, y)$ in Equation 2, and assume it is constant across the detector: $\beta_0(x, y) = \beta_0$. With this assumption, we need a single known absorption

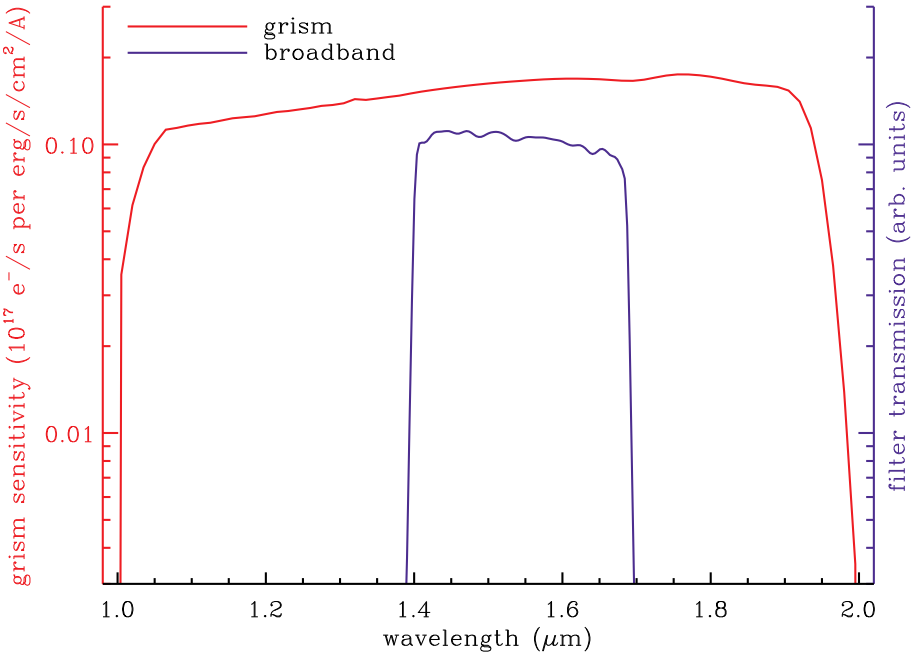

Figure 4: Assumed sensitivity functions (J. Colbert, priv. comm.). We show the grism (red) and the broadband (blue) sensitivity curves. The colored axes correspond to the sensitivity curves of the same color. We omit the study of the higher order spectral traces, as there is little information available on their properties.

Table 2: WFI Properties

dark current† ($\mathcal{D}$)	0.015 e$^-$ s^{-1} pix^{-1}
read noise† ($\mathcal{R}$)	20 e$^-$
pixel scale† (p)	$0\farcs11$ pix^{-1}
pixel array† ($n_x \times n_y$)	4096×4096 pix
wavelength range* ($\lambda_0 - \lambda_1$)	$1 - 2$ μm
dispersion* ($\delta\lambda$)	10.764 Å pix^{-1}

†These values are taken from https://wfirst.ipac.caltech.edu/sims/Param_db.html.
*We choose these values based on the anticipated design.

line, which we take to be Paschen β (Paβ: $\lambda = 1.2818072$ μm). However we must still demonstrate that the wavelength of Paβ can be measured to the precision required by the redshift requirements mentioned above.

The quality of one-dimensional spectrum extracted from a set of slitless spectroscopic images can be improved by the observational setup. Ryan, Casertano, & Pirzkal (2018) show that one can obtain a self-consistent set of spectra, corrected for contamination, when multiple orients are present. Additionally, Brammer *et al.* (2012) devise a custom 2×2 dither pattern that effectively interlaces the two-dimensional spectroscopic images. These effects conspire to improve the spectral resolution (see Ryan, Casertano, & Pirzkal 2018) in much the same way that the optimal dither pattern improves the sampling of the PSF and facilitates subsampling the rectified images (such as the drizzle algorithm for HST imaging; Fruchter & Hook 2002).

Based on these considerations, we recommend that multiple orients will likely be needed for the nominal calibration field. However, the properties of the optimal dither pattern may be subject to changes as the distortion for the detectors is better understood. Therefore we consider a basic calibration plan, where we have eight independent exposures with orients separated by 45°, fully spanning $[0°, 360°)$. This gives a total of 8×350 s of exposure time.

We extract the spectra for 216 stars from the collection of eight orients using the `LINEAR` package, again using the default configuration in Appendix A. We optimize the regularization parameter by a few steps around the standard L-curve (e.g. Hansen 1992), see Ryan, Casertano, & Pirzkal (2018) for a concrete description of this procedure. Although there are 216 cluster members in the field, only 105 stars are observed in a single WFI detector with 4/8 the orients, which is needed to provide high fidelity spectra. So, the calibration plan based on M67 can provide a reliable sampling multiplexing of $\gtrsim$100 with respect to that for WFC3/IR. In Figure 5, we show an example of a K3.7V star with $H = 15.1$ mag. The main panel shows the Kurucz model (gray line — binned for clarity) and `LINEAR` reconstruction (black). The pink region indicates the coverage around the Paβ line that is shown in more detail in the inset to the lower right. Based on a Gaussian fit to the Paβ line (shown in red in the inset), we estimate an observed wavelength of $\lambda(\text{Pa}\beta) = 1.28181$ μm, which gives a percent error of $\sim 0.027\%$. By repeating this analysis for the 105 stars extractable in this detector, we find the typical percent error is $\sim 0.01\%$ (see Figure 6), which is roughly $\sim 10\times$ smaller than the tolerance required by Spergel *et al.* (2015).

5 Conclusions and Final Remarks

We foresee several modifications to our proposed plan that may improve various aspects of the calibration, however we leave their details to future discussion. First, it may be possible to select different clusters with different ages or metallicities to improve the strength or purity of the absorption lines. This may also provide a more favorable source density, both for the WFI detector in question and the entirety of the array. Although we have considered overlapping traces as defined by the geometry of M67, it may be worth considering what is the maximal source density that is viable and still result in robust calibration.

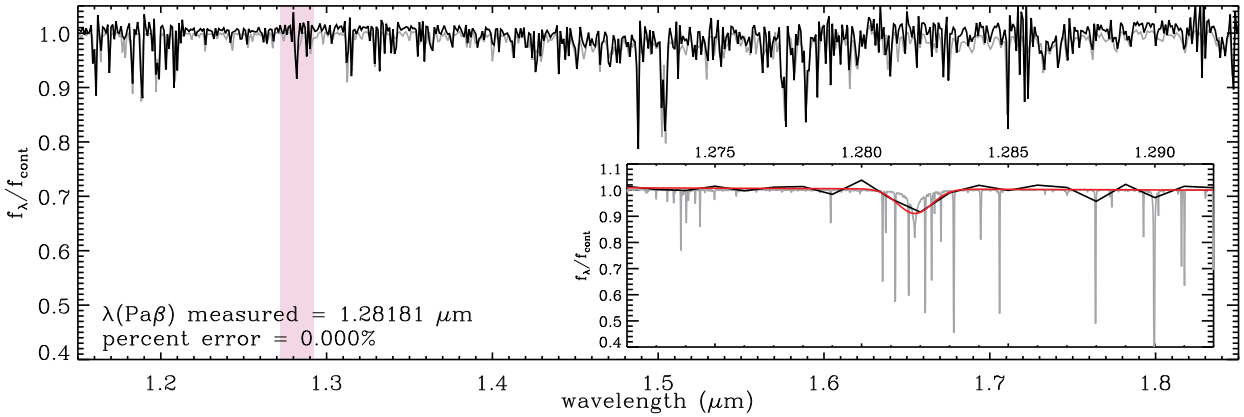

Figure 5: Simulated spectrum of a selected M67 cluster member. In the main panel, we show the Kurucz model spectrum in gray (binned for clarity) and the `LINEAR` extraction in black (sampled at 10 Å). The pink band highlights the zoomed-in region around Paβ that is shown in the inset in the lower right. In the inset, we show the same two spectra (but the Kurucz spectrum at full resolution) with a Gaussian model (red line) that is fit to the `LINEAR` extraction. For this source we estimate the wavelength of $\lambda(\mathrm{Pa}\beta) = 1.281810$ μm, which results in a percent error of 0.027%. Additionally, the typical percent error from the sample of 105 stars with viable spectra is $\sim$0.01% (see Figure 6).

Figure 6: The percent error for the measured the Paβ line (right). We show the precent error between the measured and true wavelength of Paβ for the 105 M67 stars as a function of their Y-band brightness. There are five sources with absolute percent errors more than 0.2% and not indicated here. Since these sources are all relatively bright, there is not an appreciable trend in percent error with magnitude.

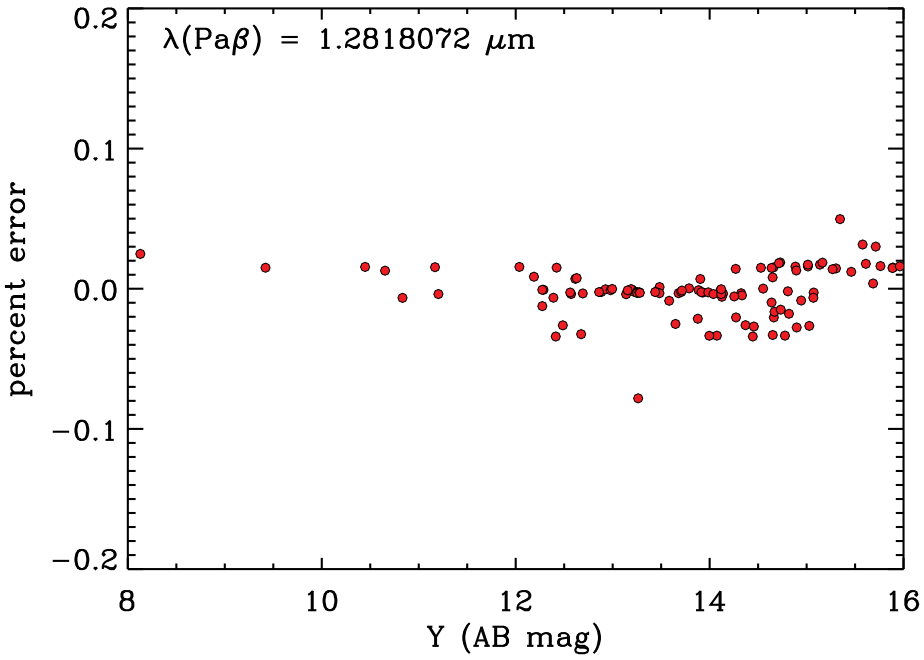

Second, the wavelength calibration is critical to the success of the spectroscopic mission, and hence should be monitored with some frequency. Therefore, a cluster/field in (or near) the continuous-viewing zones (CVZ) may provide a better calibration field, which for WFIRST will be near the ecliptic poles. This has two additional advantages: increasing the possible spacecraft orientations (which mitigates contamination and improves spectral sampling: Ryan, Casertano, & Pirzkal 2018) and decreased zodiacal background (noting that M67 is at an ecliptic latitude of $-5.^{\circ}6$; see Table 1). These tradeoffs should be considered in more detail, now that we have established that stellar absorption-line spectroscopy may be a viable calibration plan.

Above we have considered a calibration plan that requires specially collected calibration data. However, it is worth considering options that may leverage the science data collected over the life of the mission. We envision that such a plan may consist of two key components: First, since the same sources may be observed at different positions and ideally orientations, a self-calibration plan, reminiscent of *UberCal* (a photometric self-calibration for the Sloan Digital Sky Survey [SDSS]; Padmanabhan *et al.* 2008), may reduce the need for dedicated calibration data.

Second, the various follow-up surveys conducted as part of the SDSS will have a wealth of data that can be used to pre-select calibration sources amongst the science data. For example, the APO Galactic Evolution Experiment 1&2 (APOGEE) has collected spectroscopy for $\gtrsim 10^5$ stars with $H \lesssim 13$ mag in several fields (Majewski *et al.* 2017). Although these stars are distributed among the major components of the Milky Way (bulge, bar, disk, and halo), they are obviously limited to those with the usual SDSS constraint of $\delta \gtrsim -10^{\circ}$. Therefore if the HLS is observed in the south, then these SDSS-based data cannot be brought to bear, but perhaps the photometry from the Large Synoptic Survey Telescope (LSST) may be viable for calibrator selection, assuming the stellar line-of-sight velocities are sufficiently low and/or known *a priori*. Obviously, these two options are not mutually exclusive (UberCal vs. ancillary-data driven), so as the properties of the HLS are finalized, these options should be further fleshed out.

An alternative self-calibration strategy might leverage emission-line galaxies of precisely known redshifts (these redshifts may be obtained by existing facilities). We caution against this approach, since the typical spectral morphology of emission-line galaxies leads to a systematic offset in wavelength of the emission line (assuming that the emission-line region is not coincident with the continuum emission; Pirzkal *et al.* 2018). Assuming precise knowledge of the wavelength solution, Ryan & Casertano (2017) showed that this wavelength offset corresponds to a $\sim 7\%$ uncertainty in redshift. Therefore if a calibration program is built upon emission-line galaxies, then we strongly recommend that emphasis is placed on sources where the precise position of the line-emitting region (within the host galaxy) is known (such as active galactic nuclei).

We would like to thank James Colbert and David Law for helpful discussions on the WFIRST/WFI reference files and advice on SDSS-based calibration options.

6 References

Bellini, A., *et al.* 2010, A&A, 513, 50

Brammer, G. B., *et al.* 2012, ApJS, 200, 13

Fruchter, A. S. & Hook, R. N. 2002, PASP, 114, 144

Gaia Collaboration, 2018, A&A accepted, arXiv: 1804.09365

Giavalisco, M., Sahu, K., & Bohlin, R. C. 2002, WFC3-ISR, 12

Geller, A. M., Latham, D. W., & Mathieu, R. D. 2015, AJ, 150, 97

Hansen, P. C. 1992, SIAM Review, 34, 4, 561

Krone-Martins, A., *et al.* 2010, A&A, 516, 3

Kurucz, R. L. 1970, SAOSR, 39

Kurucz, R. L., & Furenlid, I. 1979, SAOSR, 387

Kurucz, R. L., & Avrett, E. H. 1981, SAOSR, 391

Majewski, S. R., *et al.* 2017, AJ, 154, 94

Oke, J. B., & Gunn, J. E. 1983, ApJ, 266, 713

Padmanabhan, N., et al. 2008, AJ, 674, 1217

Pirzkal, N., Ryan, R. E., & Brammer, G. 2016, WFC3-ISR, 15

Pirzkal, N. & Ryan, R. E., 2017, WFC3-ISR, 1

Pirzkal, N., *et al.* 2018, ApJ, submitted

Ryan, R. E., Casertano, S., & Pirzkal, N. 2018, PASP, 985, 34501

Sarajedini, A., Dotter, A., & Kirkpatrick, A. 2009, ApJ, 698, 1872

Schlafly, E. F. & Finkbeiner, D. P. 2011, ApJ, 737, 103

Spergel, D. N., *et al.* 2015, arXiv: 1503.03757

Yadav, R. K. S., *et al.* 2008, A&A, 484, 609

Appendix

A Assumed Grism Configuration

We provide the grism calibration file for completeness.

```
INSTRUMENT WFIRST
CAMERA IR
SCIENCE_EXT SCI ; Science extension
DQ_EXT DQ
ERRORS_EXT ERR
DQMASK 16383
RDNOISE 0.0
EXPTIME EXPTIME
POBJSIZE 1.0
SMFACTOR 1.0
DRZRESOLA 10.764
DRZSCALE 0.110
DRZLAMB0 10000.0
DRZROOT aXeWFC3
TELAREA 45238.93

# Detector 1; DETX=0.067,DETY=0.0
NAXIS    4096  4096
XRANGE   -200  4295

YRANGE   -2    4097
REFX   2044
REFY  -149


#-----------
#
# Beam A:
#
#-----------
BEAMA -650 650
MMAG_EXTRACT_A 30
MMAG_MARK_A 30
XOFF_A 0.0
YOFF_A 0.0
SENSITIVITY_A WFIRST_sens_test_Apr1_2016_crop.fits

#
# Trace description for Beam A:
#
DYDX_ORDER_A 0
DYDX_A_0  1

#
# Dispersion solution for Beam A:
#
DISP_ORDER_A 1
DLDP_A_0        14450.0
DLDP_A_1        10.764
```